

Metallic Interface Emerging at Magnetic Domain Wall of Antiferromagnetic Insulator — Fate of Extinct Weyl Electrons

Youhei Yamaji and Masatoshi Imada

Department of Applied Physics, University of Tokyo, Hongo, Bunkyo-ku, Tokyo, 113-8656, Japan.

Topological insulators and Chern insulators^{1,2}, in contrast to band insulators, accompany protected metallic surfaces described by Dirac-type fermions. Another peculiar metal with truncated Fermi surface called “arc” is predicted³ on the surface of zero-gap semiconductors, when Weyl fermions appear in bulk such as in iridium pyrochlore oxides $R_2\text{Ir}_2\text{O}_7$ (with rare earth elements R) under a magnetic order^{4–9}. However, the arc on the surface survives only near the all-in/all-out-type antiferromagnetic transition temperature^{7,10}. Here we show that magnetic domain walls realize novel metallic interfaces preserved by zero modes or ingap states with robust arc as a footprint of extinct Weyl electrons even in the seemingly trivial antiferromagnetic insulators. The zero modes follow a one-dimensional Dirac equation that protects ingap states, namely persisting metallicity pinned at domain walls, and maintain a ferromagnetic moment, similarly to spin/charge solitons in polyacetylene. It may solve experimental puzzles of the iridates and offers a novel quantum confinement of electrons enabling magnetic control beyond semiconductor paradigm.

Dirac/Weyl-type fermions^{11,12} realized in crystalline solids with both strong spin-orbit couplings and Coulomb repulsion are a subject of intensive studies^{10,13–16}. We elucidate another prominent effects arising from combined interaction and topology by studying single band Hubbard-type model on the pyrochlore lattice (Figure 1a), with the $J_{\text{eff}} = 1/2$ -manifold of the iridium pyrochlore oxides in mind, and show that the Weyl electrons leave behind their indelible trace with a Fermi surface at the magnetic domain walls even after the pair-annihilations of them, namely even when the Weyl electrons completely disappear and the bulk and surface turn into an insulator. This conclusion is supported by fully unrestricted Hartree-Fock calculations and Dirac equations for effective low-energy model. Electronic states bound around the domain walls are formed, whose origin is traced back to the bulk Weyl electrons. The present domain-wall theory offers insights into a number of peculiar properties of $R_2\text{Ir}_2\text{O}_7$ including weak ferromagnetism with strong field dependence⁸, bad but stubborn electronic conduction⁷ and negative magnetoresistance⁹.

The Hubbard hamiltonian with the onsite interaction U , transfer t and spin-orbit coupling ζ decoded as spin-dependent imaginary hopping at the filling of one electron per site is introduced as an effective model of iridium

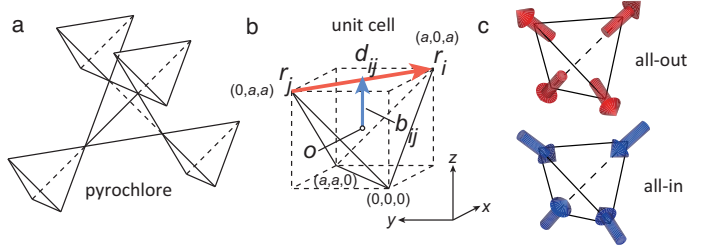


FIG. 1: Magnetic structure and notations for spin-orbit interaction on pyrochlore lattice. Pyrochlore lattice structure (a), definition of effective spin-orbit couplings on pyrochlore lattices (b), and all-in/all-out magnetic moment configuration (c). In b, vectors \vec{d}_{ij} and \vec{b}_{ij} are illustrated for a specific bond. The vector \vec{d}_{ij} points from the j -th site \vec{r}_j to the i -th site \vec{r}_i and the vector \vec{b}_{ij} points from the center of the unit tetrahedron O to the midpoint between \vec{r}_i and \vec{r}_j .

pyrochlore oxides:

$$\hat{H} = -t \sum_{i,j} \sum_{\sigma}^{\text{n.n.}} [\hat{c}_{i\sigma}^\dagger \hat{c}_{j\sigma} + \text{h.c.}] + U \sum_i \hat{n}_{i\uparrow} \hat{n}_{i\downarrow} + i\zeta \sum_{i,j}^{\text{n.n.}} \sum_{\alpha,\beta=\uparrow,\downarrow} \hat{c}_{i\alpha}^\dagger \left(\vec{\sigma} \cdot \frac{\vec{b}_{ij} \times \vec{d}_{ij}}{|\vec{b}_{ij} \times \vec{d}_{ij}|} \right)_{\alpha\beta} \hat{c}_{j\beta}, \quad (1)$$

where a fermionic operator $\hat{c}_{i\sigma}^\dagger$ ($\hat{c}_{i\sigma}$) creates (annihilates) an electron with σ -spin at i -th site. Here, the ζ term allowed by the symmetry of the pyrochlore lattice is given by pseudovectors $\vec{b}_{ij} \times \vec{d}_{ij}$ illustrated in Figure 7b.

The sign of ζ determines the electronic structure of the model^{17,18} and its ground state magnetism: The zero-gap semiconductors are realized for $\zeta < 0$ while, for $\zeta > 0$, the system becomes a topological insulator in the absence of interaction. The magnetic ground state for $\zeta < 0$ and $U > 0$ is the all-in/all-out order (Figure 1c), where the magnetic moment at each site points away from or toward the center of the tetrahedron and feels Ising-type anisotropy¹⁹. Thus, there remains two-fold degeneracy of the order.

A low-energy effective hamiltonian describing the zero-gap semiconductors on the pyrochlore lattice for $\zeta < 0$ is directly derived from the tight-binding part of the hamiltonian (1): Starting from a 8×8 Bloch hamiltonian obtained from the one-body part of equation (1), a 4×4 $\vec{k} \cdot \vec{p}$ -hamiltonian, namely, a variation of the Luttinger hamiltonian^{14,20,21} is obtained as

$$\hat{h}_{4 \times 4}(\vec{k}) = \left[+2t - 2\sqrt{2}|\zeta| \right] \mathbf{1}_4 - 2t \left[\frac{k^2}{3} \mathbf{1}_4 + \vec{d}(\vec{k}) \cdot \hat{\Gamma} \right], \quad (2)$$

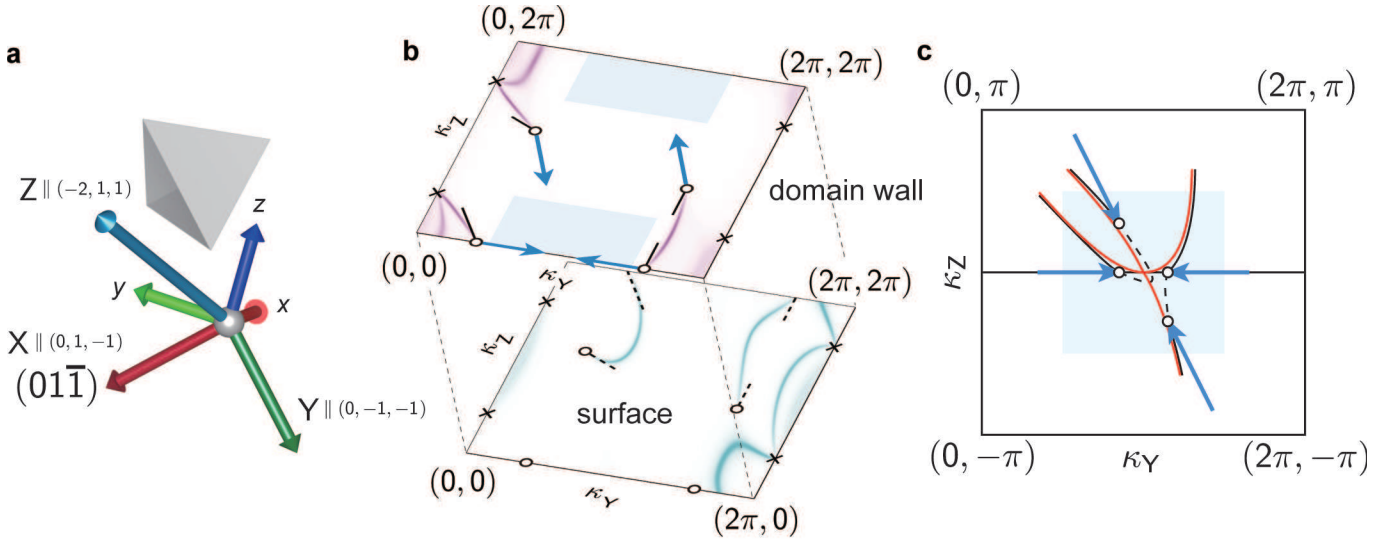


FIG. 2: **Summary of solutions for effective one-dimensional Dirac equations (3).** **a**, Newly introduced coordinate axes X , Y , and Z are illustrated for the $(01\bar{1})$ -domain wall. **b**, Zero modes of the chiral Dirac equations with low-energy $\vec{k} \cdot \vec{p}$ -hamiltonians including $\hat{h}_{(1,1,1)}^{(\pm)}$, equation (4) and $\hat{h}_{(-1,1,1)}^{(\pm)}$ (see SI). Open circles indicate the 4 Weyl points projected to the (κ_Y, κ_Z) -plane at $\vec{k}_W = \pm\sqrt{|m|/2t}(1, 1, 1)$ and $\vec{k}_W = \pm\sqrt{|m|/2t}(-1, 1, 1)$. Crosses indicate the other 4 bulk Weyl points. Solid (broken) lines represent the initial slopes of the loci of the domain-wall (surface) states starting from the Weyl points obtained from equation (3), where the full solution of equation (1) is illustrated by color contour plot. Small deviations of the black solid (broken) lines from the expectation from the contour plot may be ascribed to the small error arising from the reduction from the four-component hamiltonian (2) to the two-component hamiltonian (3), where off-diagonal elements in the order of k^2 are ignored. For $m \rightarrow 0$, solid curves shrink and disappear at $(0, 0)$. Arrows indicate the directions along which the projected Weyl points move when $|m|$ increases. **c**, Qualitative description for pair annihilation of bulk Weyl electrons on (κ_Y, κ_Z) -plane. Solid (broken) curves illustrate the loci of the domain wall (surface) zero modes. When the projected Weyl points move along the direction indicated by the arrows originally starting from $(0, 0)$, the pair annihilation occurs at $(\kappa_Y, \kappa_Z) = (\pi, 0)$. Then the closed loop of the Fermi surface on the domain walls appear, which is represented by the red solid curves. Note that the Brillouin zone is shifted $(0, \pi)$ from **b**. The shaded regions in **b** and **c** represent the same area.

where 1_4 is the identity matrix, $\vec{d}(\vec{k})^T = -\left(\frac{k_y k_z}{\sqrt{3}}, \frac{k_z k_x}{\sqrt{3}}, \frac{k_x k_y}{\sqrt{3}}, \frac{k_x^2 - k_y^2}{2\sqrt{3}}, \frac{3k_z^2 - k_x^2}{6}\right)$, and a vector of Dirac matrices $\hat{\Gamma}^T = (\hat{\Gamma}^1, \hat{\Gamma}^2, \hat{\Gamma}^3, \hat{\Gamma}^4, \hat{\Gamma}^5)$, which give time-reversal-symmetric terms for the Hilbert space of the 4×4 hamiltonian (see Methods and §I in Supplementary Information (SI) for the notations and the derivations).

Under time-reversal symmetry-breaking perturbations represented by Dirac matrices, $\hat{\Gamma}^{ab} = [\hat{\Gamma}^a, \hat{\Gamma}^b]/2i$, where $a, b = 1, 2, 3, 4, 5$ and $a \neq b$, the zero-gap semiconductor described by $\hat{h}_{4 \times 4}(\vec{k})$ offers a variety of Weyl electrons. A well-known example is all-in/all-out mean-field order parameter given by $-m[\hat{\Gamma}^5, \hat{\Gamma}^4]/2i$. This term arises from the Hartree-Fock decoupling of the U term in equation (1), and given by $m = Um_{\text{all}}/2$ with the amplitude of magnetization at each site m_{all} . The condition for the existence of gapless excitations at \vec{k} under the perturbation proportional to $\hat{\Gamma}^{ab}$ are given by $d_a(\vec{k}) = d_b(\vec{k}) = 0$ at $|\vec{k}| = \sqrt{3|m|/2t}$. Especially, for the all-in/all-out orders, 8 Weyl points $\vec{k} = \sqrt{|m|/2t}(\pm 1, \pm 1, \pm 1)^T$ emerge (see §II of SI).

As elucidated in the literature^{3,22}, bulk Weyl electrons result in Fermi arcs on surfaces and/or domain walls of the bulk crystals. By using a $\vec{k} \cdot \vec{p}$ -type perturbation theory around the Weyl points based on equation (2), we can sketch the Fermi arcs not only on the surfaces but also on the magnetic domain walls, in the following.

For simplicity, we concentrate on a pair of Weyl points, $\vec{k}_W = \pm\sqrt{|m|/2t}(1, 1, 1)^T$, and on a surface or domain wall perpendicular to $(0, +1, -1)$, namely, $(01\bar{1})$ -surface or domain wall. In the following discussion, we call a coordination axis along $(0, +1, -1)$ as X -axis (for definitions of new coordinates, see Figure 2a and Methods). Around the Weyl points, the 4×4 effective hamiltonian (2) breaks up into a pair of the following two component Dirac hamiltonians $\hat{h}_{(1,1,1)}^{(+)}$ and $\hat{h}_{(1,1,1)}^{(-)}$ that describe low-energy physics in the all-out and all-in domain, with $m > 0$ and $m < 0$, respectively. (See §I of SI) For $\vec{k}_W = \pm\sqrt{|m|/2t}(1, 1, 1)^T$, the Dirac hamiltonian up to the linear order in $-i\partial_X$, $\delta\kappa_Y$, and κ_Z , is given as

$$\begin{aligned} & \hat{h}_{(1,1,1)}^{(\pm)}(-i\partial_X, \delta\kappa_Y, \kappa_Z) \\ &= 4t\kappa_Y^{(0)} \left\{ -\left(\delta\kappa_Y + \frac{\kappa_Z}{3}\right)\hat{\sigma}_0 + \frac{\kappa_Z}{3}\hat{\sigma}_x + \frac{i}{\sqrt{3}}\hat{\sigma}_y\partial_X \right\} \end{aligned}$$

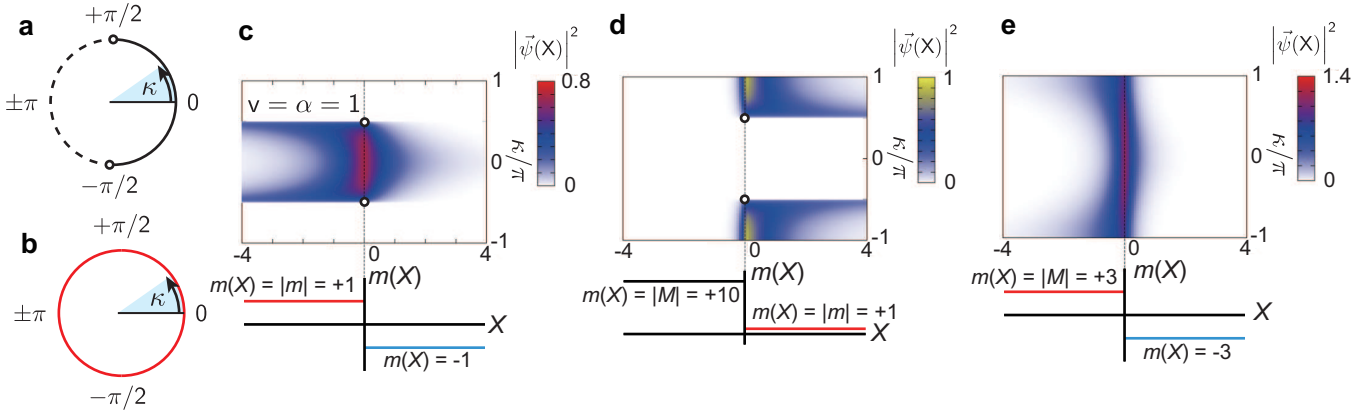


FIG. 3: **Solutions for effective one-dimensional chiral Dirac equations (4).** **a** and **b**, Simplified degrees of freedom κ corresponding to one parameter representation of loci of zero modes on (κ_Y, κ_Z) . Solid (broken) curve illustrates the loci of the domain-wall (surface) zero modes. White circles indicate the Weyl points. **a** represents the case before the pair-annihilation of the Weyl points, corresponding to **c** and **d**. On the other hand, **b** after the pair-annihilation corresponds to **e**, where the surface loci is eaten up by the domain-wall loci and the domain-wall loci form a closed Fermi surface in the Brillouin zone. **c**, Wavefunction amplitude for a domain wall state for the chiral Dirac equation (4) with α_+ in the plane of the real space coordinate X and momentum coordinate κ , with $v = \alpha_+ = 1$ and $m(x) = -\theta(+X) + \theta(-X)$. The “arc” state at the domain wall penetrates into one side of the bulk at the Weyl points. Another degenerate “arc” state localized in the other nearby side of the domain wall, obtained with $v = 1$ and $\alpha_- = -1$, penetrates to the other side of the bulk (not shown). **d**, Wavefunction amplitude for a surface state for the chiral Dirac equation (4), with $v = \alpha = 1$ and $m(x) = \theta(+X) + 10\theta(-X)$. The “arc” is formed in the missing part of the domain-wall arc. **e**, Wavefunction amplitude for a domain wall state for the chiral Dirac equation (4), with $v = \alpha = 1$ and $m(x) = -3\theta(+X) + 3\theta(-X)$. The domain wall state now forms the closed loop of the Fermi surface without penetration into the bulk. For $|m(X)| > 2$, there are no zero modes for surfaces.

$$+ \left[\mp \left(\delta\kappa_Y + \frac{\kappa_Z}{3} + \frac{|m|}{4t\kappa_Y^{(0)}} \right) + \frac{m(X)}{4t\kappa_Y^{(0)}} \right] \hat{\sigma}_z \right\}, \quad (3)$$

where we introduced a new momentum frame $(\kappa_X, \kappa_Y = \kappa_Y^{(0)} + \delta\kappa_Y, \kappa_Z)$ defined in equation (16) with $\kappa_Y^{(0)} = \pm\sqrt{|m|/2t}$, and replaced κ_X with $-i\partial_X$ (see §I of SI for derivation). The Weyl points are projected to $(\delta\kappa_Y, \kappa_Z) = (0, 0)$.

Then the two component one-dimensional chiral Dirac equation, $\hat{h}_{(1,1,1)}^{(+)}\vec{\psi}(X) = E\vec{\psi}(X)$ gives description of bound states on the surface or domain walls by introducing suitable X -dependent “mass” terms $m(X)$ ^{23,24}. Here, the all-out (all-in) domain is described by $m(X) = +|m|$ ($m(X) = -|m|$). We also note that, if $|m|$ is large enough, the Weyl points are annihilated in pair and the bulk system becomes a trivial magnetic insulator. Therefore, the mass term, $m(X) = |m|\theta(-X) - |m|\theta(X)$, gives a description of magnetic domain wall at $X = 0$, while a surface between a “vacuum” ($X < 0$) and the bulk ($X > 0$) can be mimicked by $m(X) = |M|\theta(-X) + |m|\theta(X)$ with $|M| \gg |m|$.

Figure 2b illustrates an example how the domain-wall (solid curves) and surface (broken curves) states extend around the Weyl points (white circles) before the pair-annihilation at $(\kappa_Y, \kappa_Z) = (\pi, 0)$ shown in Figure 2c.

If the translational invariance along the domain walls is preserved, these ingap states are protected by the chiral symmetry^{2,25} of the Dirac hamiltonian particularly at a pair-annihilation point $(\pi, 0)$ (see §IV of SI), and by a

generalized chiral symmetry²⁶ at other k -points. After the pair-annihilation, only the loci of the domain-walls survive.

The essential physics of these bound states is captured by the following toy model with higher symmetry, namely, a pair of chiral Dirac equations that describe 1D AIII Chern insulators^{2,25} defined by

$$\{ [\alpha_{\pm}(1 - \cos \kappa) - m(X)] \hat{\sigma}_z + vi\hat{\sigma}_y \partial_X \} \vec{\psi}(\vec{X}) = E\vec{\psi}(\vec{X}), \quad (4)$$

where $\alpha_{\pm} = \pm\alpha$ ($\alpha > 0$) and κ represents the degrees of freedom of κ_Y and κ_Z . The two “Weyl” points appear at κ that satisfies $\alpha(1 - \cos \kappa) - m(X) = 0$ (see Figure 3).

When we approach the pair annihilation of Weyl points, the Fermi arcs are expected to shrink on the surface. On the contrary, as confirmed later numerically, the Fermi arcs on the domain walls becomes elongated by eating a part of the former arc on the surface. Furthermore, after the pair annihilation, they form a closed loop (open Fermi line connected through equivalent Brillouin zone boundaries). As is clear in the high-symmetry model (4), after the pair annihilation of the Weyl points, the surface between a vacuum and the domain is no longer a topological boundary: For a given κ , boundaries where the mass changes are classified in the terminology of the 1D Chern insulators. The topological invariant changes its sign at the domain walls, as the 1D AIII Chern insulators.

The prediction based on the simple Dirac equations is confirmed by using fully unrestricted Hartree-Fock analysis of the original hamiltonian (1) on the large super-

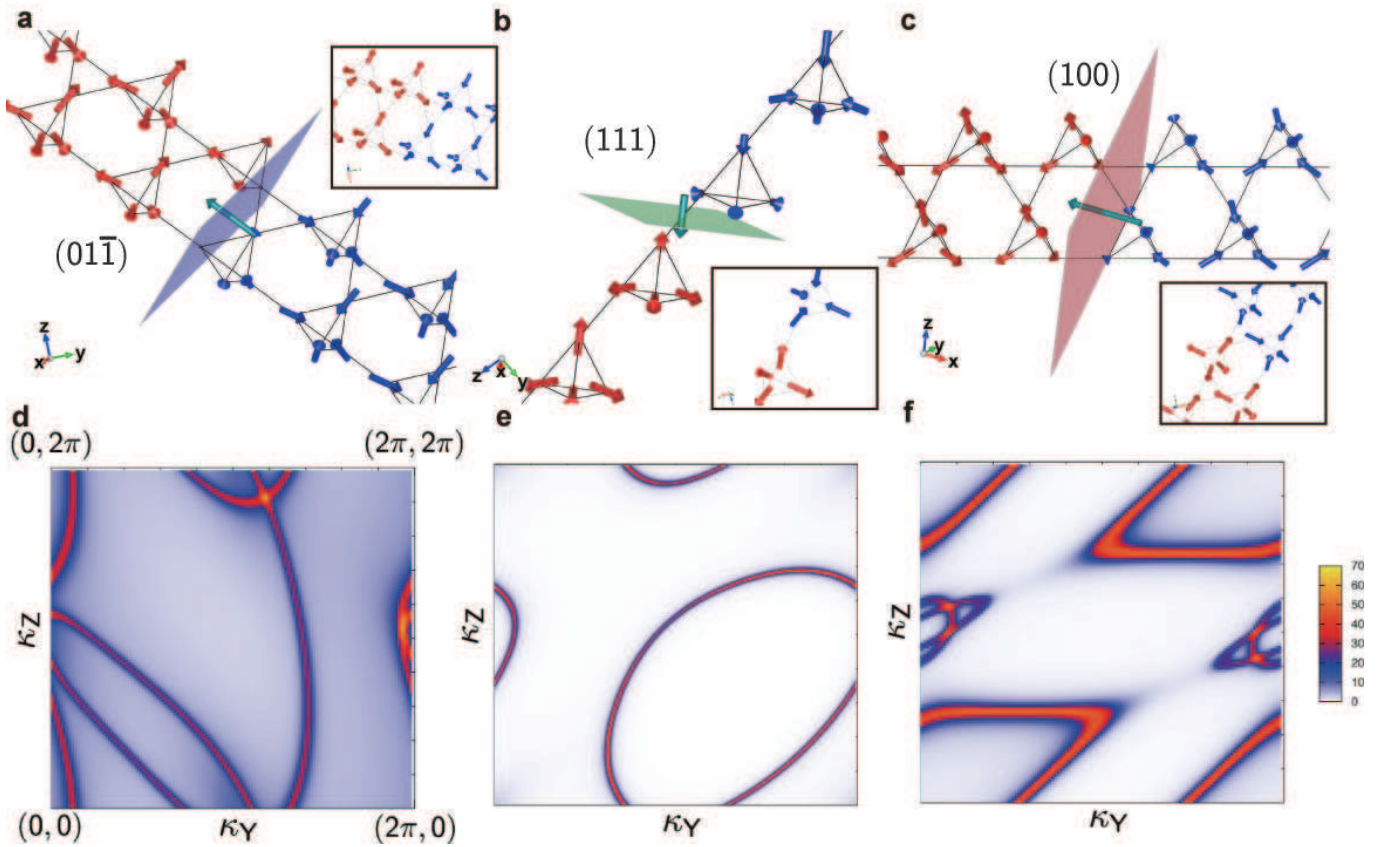


FIG. 4: **Magnetic domain walls and domain wall states.** **a-c:** Optimized magnetic structures for $(01\bar{1})$, (111) , and (100) -domain walls, obtained from initial configurations shown in the insets, for $U/t = 4$, $\zeta/t = -0.2$, and $k_B T/t = 0.1$. The length and direction of the arrows are determined by optimized unrestricted Hartree-Fock solutions. We note that only a part of the supercells nearby the domain walls are illustrated. Uniform magnetization m_0 induced around the domain walls and the intersection of the domain walls with the supercells are also illustrated as green bold arrows and shaded planes, respectively. **d-f:** Spectral functions projected to the domain walls for the $(01\bar{1})$ -domain wall (**d**), the (111) -domain wall (**e**), and the (100) -domain wall (**f**), for $k_B T/t = 0.1$, with a finite Lorentzian width $\delta = 0.01t$. At this temperature, bulk Weyl points do not exist any more. Every domain wall contributes to ingap states at the chemical potential or the Fermi level, forming open two-dimensional Fermi surfaces. As a consequence of the pair-annihilation of the Weyl points shown in Figure 2c, the Fermi arcs for the domain walls are now closed at this temperature. The complexity of the domain-wall Fermi surfaces originates from the following fact: Depending on the orientation of the domain walls, there are many choices how to connect the Weyl points with the loci of the domain-wall zero modes.

cell calculations with three different and typical domain walls, namely, $(01\bar{1})$, (100) , and (111) -domain walls, with a typical parameter set, $U/t = 4$ and $\zeta/t = -0.2$ (see Methods and SI). The self-consistent solution with optimized magnetic moment and charge distribution retains gapless domain-wall states in general and indeed on these three examples (see Figure 4).

Moreover, these domain walls show uniform magnetizations perpendicular to themselves. Surprisingly, the amplitude of these magnetizations per unit area of the domain wall does not depend on the direction of the domain wall and only depends on m within numerical errors (Figure 5a). As a result, although a single domain wall shows a uniform nonzero magnetization, a total magnetization of a closed domain wall surrounding a domain is expected to vanish. The cancellation of the domain mag-

netizations is similar to that of a pair of spin soliton and anti-soliton sandwiching a domain of polyacetylene²⁷.

The cancellation becomes, however, incomplete, when external electric fields, lattice strain, defects, charged impurities, and/or doped carriers (as we see in Figure 5b) exist. This is essentially inverse effects of magneto-strain and/or magneto-charge responses²⁸.

We find consistencies between our domain-wall theory and the experimental indications: By cooling under magnetic fields, magnetic domain walls are formed and pinned at their favorable impurity/disorder sites, thus generate a nonzero magnetization with the difference between zero and nonzero field coolings in the experiments^{5,8}. From Figure 5b, we find that n_{ex} excess carriers per unit cell induce uniform domain-wall magnetization m_0 roughly up to $\sim g\mu_B n_{\text{ex}}$, when the

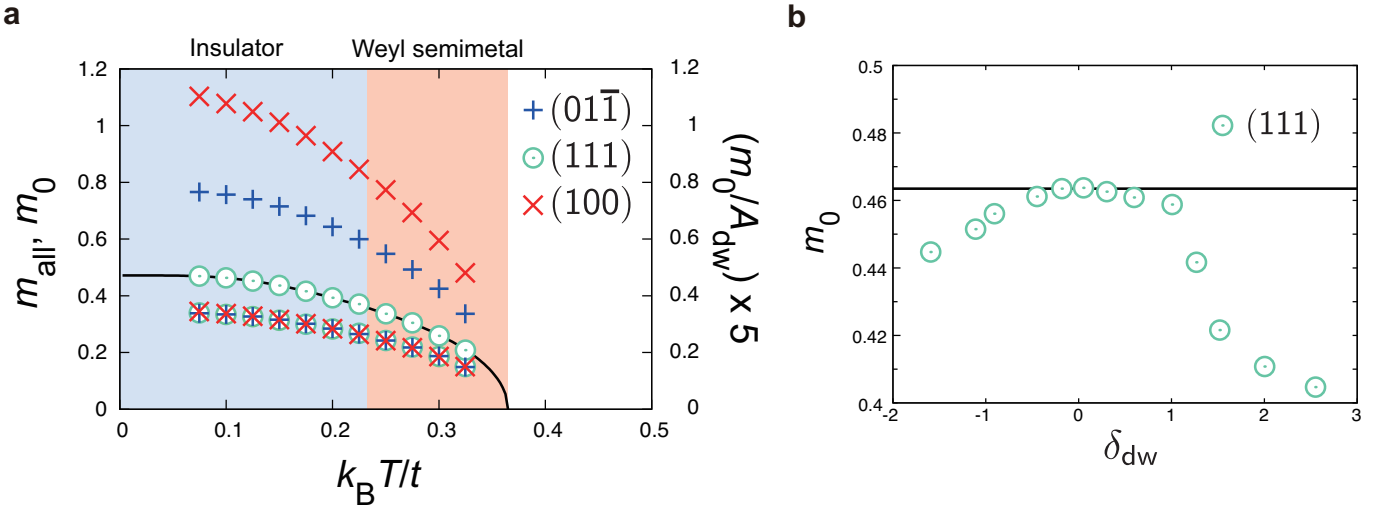


FIG. 5: **Uniform magnetization m_0 induced around the domain walls.** **a:** Uniform magnetization m_0 induced around the domain walls per supercell shown as top three symbols at each temperature for three different domain wall planes, in comparison with the bulk all-in/all-out magnetic ordered moment m_{all} (solid black curve). The uniform magnetization per unit area (a^2) of the domain walls m_0/A_{dw} is also shown as three lowest symbols at each temperature. Here the area of the intersection of a supercell with the domain walls, A_{dw} , for the (011), (111), (100)-domain wall are $8\sqrt{2}$, $4\sqrt{3}$, and 16 in units of a^2 , respectively. These three data points are almost on top of each other. **b:** Doping dependence of uniform magnetization of (111)-domain wall for $k_B T/t = 0.1$. The doping δ_{dw} is defined as increase or decrease of the electron number per present supercell around the domain walls due to changes in the chemical potential. It shows that the uniform magnetization is insensitive to the charge doping around the domain wall, within $|\delta_{\text{dw}}| < 1$. When more than one electron is doped in the supercell around the domain wall, the reduction of the uniform magnetization becomes significant with an asymmetry between electron and hole dopings.

domain wall concentration is n_{ex} (namely, the averaged domain size $\sim n_{\text{ex}}^{-1}$ unit cells). A realistic value $n_{\text{ex}} \sim 10^{-3}$ explains the peculiar uniform magnetization ($\sim 10^{-3} \mu_B/\text{unit cell}$) universally observed experimentally⁵. Self doping may also spontaneously stabilize such a stable domain structure. The smaller magnetization for polycrystals⁸ is consistent because magnetic domains are wiped out. The larger hysteresis for stoichiometric samples⁸ is simply ascribed to stronger all-in/all-out order.

The conduction on the domain wall becomes dominating at low temperatures after the elimination of the bulk Weyl electrons: Strong sample dependence⁸ and hysteresis in the magnetization sweep⁹ at lowest temperatures support this view. Our gapless electronic states are doubly degenerate and localized at the opposite side of the domain wall each other, which generate mutual scatterings and cause weak but notable Anderson localization. It is an intriguing future problem how the degeneracy is lifted. A tempting explanation of the large negative magnetoresistance for Nd/Gd compounds⁹ is the fluctuating ferromagnetic moment of Nd induced by m_0 at zero field, which scatters carriers at domain walls similarly to the double-exchange mechanism. It is desired further to understand them more quantitatively for a better magnetic control of the transport.

Methods

Unrestricted Hartree-Fock treatment. We use the

following mean-field decoupling throughout the present paper for the unrestricted Hartree-Fock (UHF) approximation:

$$\hat{n}_{i\uparrow}\hat{n}_{i\downarrow} \simeq \left[\hat{c}_{i\uparrow}^\dagger, \hat{c}_{i\downarrow}^\dagger \right] \left(\frac{\rho_i}{2} \hat{\sigma}_0 - \frac{\vec{\mu}_i \cdot \vec{\hat{\sigma}}}{2} \right) \begin{bmatrix} \hat{c}_{i\uparrow}^\dagger \\ \hat{c}_{i\downarrow}^\dagger \end{bmatrix} - \langle \hat{n}_{i\uparrow} \rangle \langle \hat{n}_{i\downarrow} \rangle + \langle \hat{c}_{i\uparrow}^\dagger \hat{c}_{i\downarrow} \rangle \langle \hat{c}_{i\downarrow}^\dagger \hat{c}_{i\uparrow} \rangle, \quad (5)$$

where the mean fields are defined as

$$\rho_i = \langle \hat{n}_{i\uparrow} \rangle + \langle \hat{n}_{i\downarrow} \rangle, \quad (6)$$

$$\mu_i^x = \langle \hat{c}_{i\uparrow}^\dagger \hat{c}_{i\downarrow} \rangle + \langle \hat{c}_{i\downarrow}^\dagger \hat{c}_{i\uparrow} \rangle, \quad (7)$$

$$\mu_i^y = -i \langle \hat{c}_{i\uparrow}^\dagger \hat{c}_{i\downarrow} \rangle + i \langle \hat{c}_{i\downarrow}^\dagger \hat{c}_{i\uparrow} \rangle, \quad (8)$$

$$\mu_i^z = \langle \hat{n}_{i\uparrow} \rangle - \langle \hat{n}_{i\downarrow} \rangle. \quad (9)$$

For instance, the all-in/all-out order is described with the spin components of the mean-fields $\vec{\mu}_i$ pointing in the configuration of all-in and all-out directions¹⁰. Here a bracket $\langle \hat{O} \rangle$ means the self-consistent average of a single particle operator \hat{O} .

Dirac matrices. Dirac matrices used in the Letter are defined as follows:

$$\hat{\Gamma}^1 = \begin{bmatrix} 0 & -i\hat{\sigma}_0 \\ +i\hat{\sigma}_0 & 0 \end{bmatrix}, \quad (10)$$

$$\hat{\Gamma}^2 = \begin{bmatrix} 0 & +\hat{\sigma}_z \\ +\hat{\sigma}_z & 0 \end{bmatrix}, \quad (11)$$

$$\hat{\Gamma}^3 = \begin{bmatrix} 0 & +\hat{\sigma}_y \\ +\hat{\sigma}_y & 0 \end{bmatrix}, \quad (12)$$

$$\hat{\Gamma}^4 = \begin{bmatrix} 0 & +\hat{\sigma}_x \\ +\hat{\sigma}_x & 0 \end{bmatrix}, \quad (13)$$

$$\hat{\Gamma}^5 = \begin{bmatrix} +\hat{\sigma}_0 & 0 \\ 0 & -\hat{\sigma}_0 \end{bmatrix}, \quad (14)$$

where $\hat{\sigma}_0$ is the two dimensional identity matrix and $\hat{\sigma}_a$ ($a = x, y, z$) are the Pauli matrices.

Domain walls. For each of three domain walls, namely, $(01\bar{1})$, (111) , and (100) -domain walls, we introduce coordinate transformations given as follows.

For the $(01\bar{1})$ -domain wall, we introduce a new oblique coordinate (X, Y, Z) with (Y, Z) parallel to the domain wall plane and corresponding momentum frame $(\kappa_X, \kappa_Y, \kappa_Z)$,

$$\vec{r} = X \begin{bmatrix} 0 \\ +2a \\ -2a \end{bmatrix} + Y \begin{bmatrix} 0 \\ -2a \\ -2a \end{bmatrix} + Z \begin{bmatrix} -4a \\ +2a \\ +2a \end{bmatrix}, \quad (15)$$

and

$$\vec{k} = \kappa_X \begin{bmatrix} 0 \\ +1/4a \\ -1/4a \end{bmatrix} + \kappa_Y \begin{bmatrix} -1/4a \\ -1/4a \\ -1/4a \end{bmatrix} + \kappa_Z \begin{bmatrix} -1/4a \\ 0 \\ 0 \end{bmatrix}. \quad (16)$$

For the (111) -domain wall,

$$\vec{r} = X \begin{bmatrix} -2a \\ 0 \\ -2a \end{bmatrix} + Y \begin{bmatrix} -2a \\ +2a \\ 0 \end{bmatrix} + Z \begin{bmatrix} 0 \\ +2a \\ -2a \end{bmatrix}, \quad (17)$$

and

$$\vec{k} = \kappa_X \begin{bmatrix} -1/4a \\ -1/4a \\ -1/4a \end{bmatrix} + \kappa_Y \begin{bmatrix} -1/4a \\ +1/4a \\ +1/4a \end{bmatrix} + \kappa_Z \begin{bmatrix} +1/4a \\ +1/4a \\ -1/4a \end{bmatrix}. \quad (18)$$

For the (100) -domain wall,

$$\vec{r} = X \begin{bmatrix} +2a \\ +2a \\ 0 \end{bmatrix} + Y \begin{bmatrix} 0 \\ +4a \\ +4a \end{bmatrix} + Z \begin{bmatrix} 0 \\ 0 \\ +4a \end{bmatrix}, \quad (19)$$

and

$$\vec{k} = \kappa_X \begin{bmatrix} +1/2a \\ 0 \\ 0 \end{bmatrix} + \kappa_Y \begin{bmatrix} -1/4a \\ +1/4a \\ 0 \end{bmatrix} + \kappa_Z \begin{bmatrix} +1/4a \\ -1/4a \\ +1/4a \end{bmatrix}.$$

¹ Hasan, M. Z. & Kane, C. L. Colloquium: Topological insulators. *Rev. Mod. Phys.* **82**, 3045-3067 (2010).

² Ryu, S., Schnyder, A. P., Furusaki, A. & Ludwig, A. W. W. Topological insulators and superconductors: tenfold

Supercells For fully unrestricted Hartree-Fock calculations, we use supercells to describe domain walls.

For the $(01\bar{1})$ -domain wall calculations, we specify the sites within the supercell as

$$\vec{r}_{n\ell L} = \vec{r}_n + \ell \begin{bmatrix} -2a \\ +2a \\ +0 \end{bmatrix} + L \begin{bmatrix} 0 \\ +2a \\ -2a \end{bmatrix}, \quad (21)$$

where n , ℓ , and L are integers, and \vec{r}_n ($n = 1, 2, 3, 4$) is the location of the n -th site in the unit cell: $\vec{r}_1 = (a, 0, a)^T$, $\vec{r}_2 = (0, a, a)^T$, $\vec{r}_3 = (a, a, 0)^T$, and $\vec{r}_4 = (0, 0, 0)^T$.

For the the (111) -domain wall,

$$\vec{r}_{n0L} = \vec{r}_n + L \begin{bmatrix} -2a \\ 0 \\ -2a \end{bmatrix}, \quad (22)$$

and, for the (100) -domain wall,

$$\vec{r}_{n\ell L} = \vec{r}_n + \ell \begin{bmatrix} -2a \\ +2a \\ +0 \end{bmatrix} + L \begin{bmatrix} +2a \\ +2a \\ 0 \end{bmatrix}. \quad (23)$$

For actual unrestricted Hartree-Fock calculations, we chose $\ell = 0, 1$ and $L = 0, 1, \dots, 39$. We make sharp domain walls between $L = 19$ and $L = 20$ as the initial conditions. We use periodic boundary conditions parallel to the domain walls, and open boundary conditions perpendicular to the domain walls.

YY thanks Moyuru Kurita for enlightening discussion in the early stage of the present study. YY also thanks Takahiro Misawa for his comments on the topological classification of the 1D Dirac equations. This work is financially supported by MEXT HPCI Strategic Programs for Innovative Research (SPIRE) and Computational Materials Science Initiative (CMSI). Numerical calculation was partly carried out at the Supercomputer Center, Institute for Solid State Physics, Univ. of Tokyo. This work was also supported by Grant-in-Aid for Scientific Research (No. 22104010, No. 22340090, and No. 23740261) from MEXT, Japan.

way and dimensional hierarchy. *New J. Phys.* **12**, 065010 (2010).

³ Wan, X., Turner, A. M., Vishwanath, A. & Savrasov, S. Y. Topological semimetal and Fermi-arc surface states in

the electronic structure of pyrochlore iridates. *Phys. Rev. B* **83**, 205101 (2011).

⁴ Yanagishima, D. & Maeno, Y. Metal-Nonmetal Changeover in Pyrochlore Iridates. *J. Phys. Soc. Jpn.* **70**, 2880-2883 (2001).

⁵ Matsuhira, K., Wakushima, M., Hinatsu, Y. & Takagi, S. Metal-Insulator Transitions in Pyrochlore Oxides $Ln_2Ir_2O_7$. *J. Phys. Soc. Jpn.* **80**, 094701 (2011).

⁶ Tomiyasu, K., Matsuhira, K., Iwasa, K., Watahiki, M., Takagi, S., Wakushima, M., Hinatsu, Y., Yokoyama, M., Ohoyama, K. & Yamada, K. Emergence of magnetic long-range order in frustrated pyrochlore $Nd_2Ir_2O_7$ with Metal-Insulator Transition. *J. Phys. Soc. Jpn.* **81**, 034709 (2012).

⁷ Ueda, K., Fujioka, J., Takahashi, Y., Suzuki, T., Ishiwata, S., Taguchi, Y. & Tokura, Y. Variation of charge dynamics in the course of metal-insulator transition for pyrochlore-type $Nd_2Ir_2O_7$. *Phys. Rev. Lett.* **109**, 136402 (2012).

⁸ Ishikawa, J. J., O'Farrell, E. C. T. & Nakatsuji, S. Continuous transition between antiferromagnetic insulator and paramagnetic metal in the pyrochlore iridate $Eu_2Ir_2O_7$. *Phys. Rev. B* **85**, 245109 (2012).

⁹ Matsuhira, K., Tokunaga, M., Wakushima, M., Hinatsu, Y. & Takagi, S. Giant magnetoresistance effect in the metal-insulator transition of pyrochlore oxide $Nd_2Ir_2O_7$. *J. Phys. Soc. Jpn.* **82**, 023706 (2013).

¹⁰ Witczak-Krempa, W. & Kim, Y.-B. Topological and magnetic phases of interacting electrons in the pyrochlore iridates. *Phys. Rev. B* **85**, 045124 (2012).

¹¹ Abrikosov, A. A. & Beneslavskii, S. D. Possible existence of substances intermediate between metals and dielectrics. *Sov. Phys. JETP* **32**, 699 (1971) [*Zh. Eksp. Teor. Fiz.* **59**, 1280 (1970)].

¹² Lifshitz, E. M. & Pitaevskii, L. P. *Statistical Physics, Part 2*, (Oxford, 2002).

¹³ Castro Neto, A. H., Guinea, F., Peres, N. M. R., Novoselov, K. S. & Geim, A. K. The electronic properties of graphene. *Rev. Mod. Phys.* **81**, 109-162 (2009).

¹⁴ Moon, E.-G., Xu, C., Kim, Y. B. & Balents, L. Non-Fermi liquid and topological states with strong spin-orbit coupling. Preprint at <http://arxiv.org/abs/1212.1168v1>.

¹⁵ Pesin, D. & Balents, L. Mott physics and hand topology in materials with strong spin-orbit interaction. *Nature Phys.* **6**, 376-381 (2010).

¹⁶ Go, A., Witczak-Krempa, W., Jeon, G. S., Park, K. & Kim, Y.-B. Correlation effects on 3D topological phases: From bulk to boundary. *Phys. Rev. Lett.* **109**, 066401 (2012).

¹⁷ Guo, H.-M. & Franz, M. Three-dimensional topological insulators on the pyrochlore lattice. *Phys. Rev. Lett.* **103**, 206805 (2009).

¹⁸ Kurita, M., Yamaji, Y. & Imada, M. Topological insulators from spontaneous symmetry breaking induced by electron correletion on pyrochlore lattices. *J. Phys. Soc. Jpn.* **80**, 044708 (2011).

¹⁹ Elhajal, M., Canals, B., Sunyer, R. & Lacroix, C. Ordering in the pyrochlore antiferromagnet due to Dzyaloshinsky-Moriya interactions. *Phys. Rev. B* **71**, 094420 (2005).

²⁰ Luttinger, J. M. Quantum theory of cyclotron resonance in semiconductors: general theory. *Phys. Rev.* **102**, 1030-1041 (1956).

²¹ Murakami, S., Nagaosa, N. & Zhang, S.-C. SU(2) non-Abelian holonomy and dissipationless spin current in semiconductors. *Phys. Rev. B* **69**, 235206 (2004).

²² Silaev, M. A. & Volovik, G. E. Topological Fermi arcs in superfluid 3He . *Phys. Rev. B* **86**, 214511 (2012).

²³ Jackiw, R. & Rebbi, C. Solitons with fermion number 1/2. *Phys. Rev. D* **13**, 3398 (1976).

²⁴ Zhang, F., Kane, C. L. & Mele, E. J. Surface states of topological insulators. *Phys. Rev. B* **86**, 081303(R) (2012).

²⁵ Teo, J. C. Y. & Kane, C. L. Topological defects and gapless modes in insulators and superconductors. *Phys. Rev. B* **82**, 115120 (2010).

²⁶ Kawarabayashi, T., Hatsugai, Y., Morimoto, T. & Aoki, H. Generalized chiral symmetry and stability of zero modes for tilted Dirac cones. *Phys. Rev. B* **83**, 153414 (2011).

²⁷ Heeger, A. J., Kivelson, S., Schrieffer, J. R. & Su, W.-P. Solitons in conducting polymers. *Rev. Mod. Phys.* **60**, 781-850 (1988).

²⁸ Arima, T. Time-reversal symmetry breaking and consequent physical responses induced by all-in/all-out type magnetic order on the pyrochlore lattice. *J. Phys. Soc. Jpn.* **82**, 013705 (2013).

Supplementary Information

I. DERIVATION OF LOW ENERGY HAMILTONIAN

We study Weyl electrons by using the hamiltonian (1), which describes hole states of the $J_{\text{eff}} = 1/2$ -manifold of iridium atoms. After the decoupling Eq.(5), and using the unrestricted Hartree-Fock solution of Eq.(1) given by the all-in/all-out magnetic order, we replace the U term with the mean-field one with the order parameter m .

We begin with a Fourier transformed form of the Hartree-Fock hamiltonian given by a 8×8 hamiltonian. By extracting a low energy Hilbert space around the Fermi level, it is reduced to a 6×6 hamiltonian. If we use k -group terminology at the Γ point, we extract $T_{2g} \otimes E_{1/2}$ -manifold of a double group T_d from $(T_{2g} \oplus A_{1g}) \otimes E_{1/2}$.

Next we further extract a 4×4 low-energy part of the 6×6 effective hamiltonian. This corresponds to extraction of the $G_{3/2}$ -manifold (or $J_{3/2}$ -manifold) from $T_{2g} \otimes E_{1/2} = E_{5/2} \oplus G_{3/2}$, in the k -group terminology.

A. 8×8 hamiltonian

The Fourier transformed form of 8×8 hamiltonian (1) after the Hartree-Fock approximation is given by

$$\hat{H}_0(\vec{k}) = \sum_k \sum_{\nu=1, \dots, 4} \sum_{\alpha, \beta=\uparrow, \downarrow} \hat{c}_{\vec{k}\nu\alpha}^\dagger \hat{\mathcal{H}}_0 \hat{c}_{\vec{k}\mu\beta}, \quad (\text{S.1})$$

and $\hat{\mathcal{H}}_0 = \hat{\mathcal{K}}_0 + \hat{\mathcal{Z}}_0 + \hat{\mathcal{M}}_0$ with $\hat{\mathcal{K}}_0$ being the kinetic term proportional to t as

$$\hat{\mathcal{K}}_0(\vec{k}) = -2t\hat{\sigma}_0 \begin{bmatrix} 0 & \cos(k_x - k_y) & \cos(k_y - k_z) & \cos(k_z + k_x) \\ \cos(k_x - k_y) & 0 & \cos(k_z - k_x) & \cos(k_y + k_z) \\ \cos(k_y - k_z) & \cos(k_z - k_x) & 0 & \cos(k_x + k_y) \\ \cos(k_z + k_x) & \cos(k_y + k_z) & \cos(k_x + k_y) & 0 \end{bmatrix}, \quad (\text{S.2})$$

$\hat{\mathcal{Z}}_0$ being the spin-orbit term proportional to ζ as

$$\hat{\mathcal{Z}}_0(\vec{k}) = 2i\zeta \begin{bmatrix} 0 & +\frac{\hat{\sigma}_x + \hat{\sigma}_y}{\sqrt{2}} \cos(k_x - k_y) & -\frac{\hat{\sigma}_y + \hat{\sigma}_z}{\sqrt{2}} \cos(k_y - k_z) & +\frac{\hat{\sigma}_z - \hat{\sigma}_x}{\sqrt{2}} \cos(k_z + k_x) \\ -\frac{\hat{\sigma}_x + \hat{\sigma}_y}{\sqrt{2}} \cos(k_x - k_y) & 0 & +\frac{\hat{\sigma}_z + \hat{\sigma}_x}{\sqrt{2}} \cos(k_z - k_x) & +\frac{\hat{\sigma}_y - \hat{\sigma}_z}{\sqrt{2}} \cos(k_y + k_z) \\ +\frac{\hat{\sigma}_y + \hat{\sigma}_z}{\sqrt{2}} \cos(k_y - k_z) & -\frac{\hat{\sigma}_z + \hat{\sigma}_x}{\sqrt{2}} \cos(k_z - k_x) & 0 & +\frac{\hat{\sigma}_x - \hat{\sigma}_y}{\sqrt{2}} \cos(k_x + k_y) \\ -\frac{\hat{\sigma}_z - \hat{\sigma}_x}{\sqrt{2}} \cos(k_x + k_z) & -\frac{\hat{\sigma}_y - \hat{\sigma}_z}{\sqrt{2}} \cos(k_y + k_z) & -\frac{\hat{\sigma}_x - \hat{\sigma}_y}{\sqrt{2}} \cos(k_x + k_y) & 0 \end{bmatrix} \quad (\text{S.3})$$

and $\hat{\mathcal{M}}_0$ being the Hartree-Fock term of the all-in/all-out magnetic order proportional to m

$$\hat{\mathcal{M}}_0 = \frac{m}{\sqrt{3}} \begin{bmatrix} +\hat{\sigma}_x - \hat{\sigma}_y + \hat{\sigma}_z & 0 & 0 & 0 \\ 0 & -\hat{\sigma}_x + \hat{\sigma}_y + \hat{\sigma}_z & 0 & 0 \\ 0 & 0 & +\hat{\sigma}_x + \hat{\sigma}_y - \hat{\sigma}_z & 0 \\ 0 & 0 & 0 & -\hat{\sigma}_x - \hat{\sigma}_y - \hat{\sigma}_z \end{bmatrix}. \quad (\text{S.4})$$

B. Reduction from 8×8 to 6×6 hamiltonian

with

By assuming $|\zeta|/t, m/t, k^2 \ll 1$, the leading order terms of the 6×6 low energy effective hamiltonian $\hat{\mathcal{H}}_1 = \hat{\mathcal{K}}_1 + \hat{\mathcal{Z}}_1 + \hat{\mathcal{M}}_1$ is extracted by using a projection,

$$\hat{\mathcal{P}}_{4 \times 3} = \frac{1}{2} \begin{bmatrix} +1 & -1 & +1 \\ -1 & +1 & +1 \\ +1 & +1 & -1 \\ -1 & -1 & -1 \end{bmatrix} \quad (\text{S.5})$$

$$\begin{aligned} \hat{\mathcal{K}}_1 &= \hat{\mathcal{P}}_{4 \times 3}^T \hat{\mathcal{K}}_0 \hat{\mathcal{P}}_{4 \times 3} = \\ &= -2t\hat{\sigma}_0 \left(\cos k_x \cos k_y \begin{bmatrix} -1 & 0 & 0 \\ 0 & -1 & 0 \\ 0 & 0 & +1 \end{bmatrix} + \cos k_y \cos k_z \begin{bmatrix} +1 & 0 & 0 \\ 0 & -1 & 0 \\ 0 & 0 & -1 \end{bmatrix} + \cos k_z \cos k_x \begin{bmatrix} -1 & 0 & 0 \\ 0 & +1 & 0 \\ 0 & 0 & -1 \end{bmatrix} \right) \\ &\quad -2t\hat{\sigma}_0 \begin{bmatrix} 0 & \sin k_x \sin k_y & \sin k_z \sin k_x \\ \sin k_x \sin k_y & 0 & \sin k_y \sin k_z \\ \sin k_z \sin k_x & \sin k_y \sin k_z & 0 \end{bmatrix} \\ &= -2t\hat{\sigma}_0 \begin{bmatrix} -1 + k_x^2 & k_x k_y & k_x k_z \\ k_y k_x & -1 + k_y^2 & k_y k_z \\ k_z k_x & k_z k_y & -1 + k_z^2 \end{bmatrix} + \mathcal{O}(k^3) = 2t\mathbf{1}_6 - 2t(\vec{k}\hat{\sigma}_0) \otimes (\vec{k}\hat{\sigma}_0) + \mathcal{O}(k^3), \end{aligned} \quad (\text{S.6})$$

and

$$\hat{\mathcal{Z}}_1 = \hat{\mathcal{P}}_{4 \times 3}^T \hat{\mathcal{Z}}_0 \hat{\mathcal{P}}_{4 \times 3} = 2\sqrt{2}i\zeta \begin{bmatrix} 0 & -\hat{\sigma}_z & +\hat{\sigma}_y \\ +\hat{\sigma}_z & 0 & -\hat{\sigma}_x \\ -\hat{\sigma}_y & +\hat{\sigma}_x & 0 \end{bmatrix} + \mathcal{O}(\zeta k^2). \quad (\text{S.7})$$

The all-in/all-out mean field $\hat{\mathcal{M}}_0$ is projected to the low-energy subspace as

$$\hat{\mathcal{M}}_1 = \hat{\mathcal{P}}_{4 \times 3}^T \hat{\mathcal{M}}_0 \hat{\mathcal{P}}_{4 \times 3} = \frac{m}{\sqrt{3}} \begin{bmatrix} 0 & \hat{\sigma}_z & \hat{\sigma}_y \\ \hat{\sigma}_z & 0 & \hat{\sigma}_x \\ \hat{\sigma}_y & \hat{\sigma}_x & 0 \end{bmatrix}. \quad (\text{S.8})$$

C. Reduction from 6×6 to 4×4

Then, we extract a 4×4 -hamiltonian from $\hat{\mathcal{H}}_1$ by using a unitary transformaion consisting of irreducible representation $E_{5/2}$ and $G_{3/2}$ of the double group T_d ,

$$\hat{\mathcal{U}}_J = \begin{bmatrix} -\frac{1}{\sqrt{3}}\hat{\sigma}_x & -\frac{1}{\sqrt{2}}\hat{\sigma}_z & +\frac{i}{\sqrt{6}}\hat{\sigma}_y \\ -\frac{1}{\sqrt{3}}\hat{\sigma}_y & -\frac{1}{\sqrt{2}}\hat{\sigma}_0 & -\frac{i}{\sqrt{6}}\hat{\sigma}_x \\ -\frac{1}{\sqrt{3}}\hat{\sigma}_z & 0 & +\frac{2}{\sqrt{6}}\hat{\sigma}_0 \end{bmatrix}. \quad (\text{S.9})$$

The 1st and 2nd column of $\hat{\mathcal{U}}_J$ correspond to the $E_{5/2}$ -irreducible representation, and the other columns correspond to the $G_{3/2}$ -irreducible representation. Then, the kinetic term \mathcal{K}_1 is transformed as follows:

$$\hat{\mathcal{U}}_J^\dagger \hat{\mathcal{K}}_1 \hat{\mathcal{U}}_J = 2t\mathbf{1}_6 - 2t\hat{\mathcal{U}}_J^\dagger (\vec{k}\hat{\sigma}_0) \otimes (\vec{k}\hat{\sigma}_0) \hat{\mathcal{U}}_J = 2t\mathbf{1}_6 - 2t \begin{bmatrix} \frac{1}{3}k^2\hat{\sigma}_0 & \vec{\nu}^\dagger(\vec{k}) \\ \vec{\nu}(\vec{k}) & \hat{\kappa}(\vec{k}) \end{bmatrix}, \quad (\text{S.10})$$

where

$$\vec{\nu}^\dagger(\vec{k}) = \left(\frac{k_z k_x}{\sqrt{6}}\hat{\sigma}_0 + i\frac{k_y k_z}{\sqrt{6}}\hat{\sigma}_z - i\frac{k_x^2 - k_y^2}{\sqrt{6}}\hat{\sigma}_y + i\frac{2k_x k_y}{\sqrt{6}}, \frac{k^2 - 3k_z^2}{3\sqrt{2}}\hat{\sigma}_z - \frac{k_z k_x}{\sqrt{2}}\hat{\sigma}_x - \frac{k_y k_z}{\sqrt{2}}\hat{\sigma}_y \right), \quad (\text{S.11})$$

and

$$\hat{\kappa}(\vec{k}) = \begin{bmatrix} \frac{k_x^2 + k_y^2}{2}\hat{\sigma}_0 & -\frac{k_x^2 - k_y^2}{2\sqrt{3}}\hat{\sigma}_x - \frac{k_x k_y}{\sqrt{3}}\hat{\sigma}_y - \frac{k_z k_x}{\sqrt{3}}\hat{\sigma}_z - i\frac{k_y k_z}{\sqrt{3}}\hat{\sigma}_0 \\ -\frac{k_x^2 - k_y^2}{2\sqrt{3}}\hat{\sigma}_x - \frac{k_x k_y}{\sqrt{3}}\hat{\sigma}_y - \frac{k_z k_x}{\sqrt{3}}\hat{\sigma}_z - i\frac{k_y k_z}{\sqrt{3}}\hat{\sigma}_0 & \frac{k^2 + 3k_z^2}{6}\hat{\sigma}_0 \end{bmatrix}. \quad (\text{S.12})$$

The effective spin-orbit coupling and the all-in/all-out mean field are transformed as

$$\tilde{\mathcal{Z}}_2 = \hat{\mathcal{U}}_J^\dagger \hat{\mathcal{Z}}_1 \hat{\mathcal{U}}_J = 2\sqrt{2}\zeta \begin{bmatrix} -2 \times \mathbf{1} & \mathbf{0} & \mathbf{0} \\ \mathbf{0} & \mathbf{1} & \mathbf{0} \\ \mathbf{0} & \mathbf{0} & \mathbf{1} \end{bmatrix}, \quad (\text{S.13})$$

and

$$\tilde{\mathcal{M}}_2 = \hat{\mathcal{U}}_J^\dagger \hat{\mathcal{M}}_1 \hat{\mathcal{U}}_J = \begin{bmatrix} \mathbf{0} & \mathbf{0} & \mathbf{0} \\ \mathbf{0} & \mathbf{0} & +im\hat{\sigma}_x \\ \mathbf{0} & -im\hat{\sigma}_x & \mathbf{0} \end{bmatrix}. \quad (\text{S.14})$$

For $\zeta < 0$, by counting the number of states, it becomes clear that the chemical potential is located within the $G_{3/2}$ -manifold to keep the electron density at half filling, in other words, one electron per site. Here, the reduction to 4×4 -hamiltonian $\hat{\mathcal{H}}_2 \equiv \hat{\mathcal{K}}_2 + \hat{\mathcal{Z}}_2 + \hat{\mathcal{M}}_2$ is achieved by ignoring the off-diagonal term $\vec{\nu}^\dagger(\vec{k})$, which generates negligible corrections of $\mathcal{O}(k^4/6\sqrt{2}|\zeta|)$. Here, $\hat{\mathcal{K}}_2 = \hat{\kappa}(\vec{k})$ while $\hat{\mathcal{Z}}_2$ and $\hat{\mathcal{M}}_2 = m\hat{\Gamma}^{54}$ are the lower right 4×4 components of $\tilde{\mathcal{Z}}_2$ and $\tilde{\mathcal{M}}_2$, respectively. We take the notation for the tight binding part as $\hat{h}_{4 \times 4} \equiv \hat{\mathcal{K}}_2 + \hat{\mathcal{Z}}_2$,

where $\hat{h}_{4 \times 4}$ can be rewritten in a compact form as

$$\hat{h}_{4 \times 4}(\vec{k}) = \left[+2t \left(1 - \frac{k^2}{3} \right) - 2\sqrt{2}|\zeta| \right] \mathbf{1}_4 - 2t\vec{d}(\vec{k}) \cdot \vec{\Gamma}, \quad (\text{S.15})$$

which is nothing but Eq.(2).

II. GREEN'S FUNCTION

By calculating Green's functions discussed below, electronic spectra for the 4×4 hamiltonian become accessible. The Green's function $\hat{G}_{4 \times 4}$ for the Bloch hamiltonian $\hat{h}_{4 \times 4}$ is defined by

$$\begin{aligned} \hat{G}_{4 \times 4}(\vec{k}, \omega)^{-1} &= (\omega + \mu)\hat{\sigma}_0 \otimes \hat{\tau}_0 - \hat{h}_{4 \times 4}(\vec{k}) - m\hat{\Gamma}^{54} \\ &= \varpi(\vec{k}, \omega)\mathbf{1}_4 + 2t\vec{d}(\vec{k}) \cdot \vec{\Gamma} - m\hat{\Gamma}^{54}, \end{aligned} \quad (\text{S.16})$$

where $\varpi(\vec{k}, \omega) = \omega + \mu - 2t + 2\sqrt{2}|\zeta| + 2tk^2/3$.

Inverting the right-hand side of Eq.(S.16), we obtain the Green's function as follows,

$$\hat{G}_{4 \times 4} = \left[\varpi\mathbf{1}_4 - 2t\vec{d} \cdot \vec{\Gamma} + m\hat{\Gamma}^{54} \right] \frac{\left[\varpi^2 - 4t^2|\vec{d}|^2 - m^2 \right] \mathbf{1}_4 - 4mt \left[d_3\hat{\Gamma}^{21} + d_2\hat{\Gamma}^{13} + d_1\hat{\Gamma}^{32} \right]}{\left[\varpi^2 - 4t^2|\vec{d}|^2 - m^2 \right]^2 - 16m^2t^2 [d_1^2 + d_2^2 + d_3^2]}$$

$$\begin{aligned}
&= \left[\frac{\mathbf{1}_4}{2} + \frac{-2t\vec{d} \cdot \vec{\hat{\Gamma}} + m\hat{\Gamma}^{54}}{2E_+} + \frac{\mathbf{1}_4}{2} - \frac{-2t\vec{d} \cdot \vec{\hat{\Gamma}} + m\hat{\Gamma}^{54}}{2E_+} \right] \left[\frac{\mathbf{1}_4}{2} - \text{sign}(m) \frac{d_3\hat{\Gamma}^{21} + d_2\hat{\Gamma}^{13} + d_1\hat{\Gamma}^{32}}{2\sqrt{d_1^2 + d_2^2 + d_3^2}} \right] \\
&+ \left[\frac{\mathbf{1}_4}{2} + \frac{-2t\vec{d} \cdot \vec{\hat{\Gamma}} + m\hat{\Gamma}^{54}}{2E_-} + \frac{\mathbf{1}_4}{2} - \frac{-2t\vec{d} \cdot \vec{\hat{\Gamma}} + m\hat{\Gamma}^{54}}{2E_-} \right] \left[\frac{\mathbf{1}_4}{2} + \text{sign}(m) \frac{d_3\hat{\Gamma}^{21} + d_2\hat{\Gamma}^{13} + d_1\hat{\Gamma}^{32}}{2\sqrt{d_1^2 + d_2^2 + d_3^2}} \right]. \quad (\text{S.17})
\end{aligned}$$

Here we omit \vec{k} - and ω -dependences above and define the functions E_{\pm} as

$$E_{\pm}(\vec{k}) = \sqrt{4t^2|\vec{d}(\vec{k})|^2 + m^2 \pm 4|m|t\sqrt{d_1(\vec{k})^2 + d_2(\vec{k})^2 + d_3(\vec{k})^2}}. \quad (\text{S.18})$$

For the above calculation of the Green's function, the following two identities are useful:

$$|\vec{d}(\vec{k})| = |\vec{k}|^2/3, \quad (\text{S.19})$$

and

$$(\vec{d}(\vec{k}) \cdot \vec{\hat{\Gamma}})^2 = |\vec{d}(\vec{k})|^2. \quad (\text{S.20})$$

Along a symmetry axis parallel to $\vec{k} = (+1, +1, +1)$, the 4×4 hamiltonian is diagonalized by the following unitary matrix,

$$\hat{\mathcal{U}}_{(1,1,1)} = \begin{bmatrix} -ai & -bi & +bi & +ai \\ -b\vartheta & +a\vartheta & -a\vartheta & +b\vartheta \\ +b\vartheta^* & -a\vartheta^* & -a\vartheta^* & +b\vartheta^* \\ +a & +b & +b & +a \end{bmatrix}, \quad (\text{S.21})$$

where

$$\vartheta = \frac{1+i}{\sqrt{2}}, \quad (\text{S.22})$$

$$a = \frac{\sqrt{\sqrt{3}+1}}{2 \cdot 3^{1/4}}, \quad (\text{S.23})$$

$$b = \frac{\sqrt{\sqrt{3}-1}}{2 \cdot 3^{1/4}}. \quad (\text{S.24})$$

It is useful to list up the unitary transformation of the matrices $\hat{\Gamma}^i$ ($i = 1, 2, 3, 4, 5$) and $m\hat{\Gamma}^{54}$:

$$\hat{\mathcal{U}}_{(1,1,1)}^{\dagger} \hat{\Gamma}^1 \hat{\mathcal{U}}_{(1,1,1)} = \begin{bmatrix} +2ab(\vartheta + \vartheta^*) & -2a^2\vartheta^* + 2b^2\vartheta & 0 & 0 \\ -2a^2\vartheta + 2b^2\vartheta^* & -2ab(\vartheta + \vartheta^*) & 0 & 0 \\ 0 & 0 & +2ab(\vartheta + \vartheta^*) & +2a^2\vartheta - 2b^2\vartheta^* \\ 0 & 0 & +2a^2\vartheta^* - 2b^2\vartheta & -2ab(\vartheta + \vartheta^*) \end{bmatrix} \quad (\text{S.25})$$

$$= \begin{bmatrix} +1/\sqrt{3} & -1/\sqrt{6} + i/\sqrt{2} & 0 & 0 \\ -1/\sqrt{6} - i/\sqrt{2} & -1/\sqrt{3} & 0 & 0 \\ 0 & 0 & +1/\sqrt{3} & +1/\sqrt{6} + i/\sqrt{2} \\ 0 & 0 & +1/\sqrt{6} - i/\sqrt{2} & -1/\sqrt{3} \end{bmatrix}, \quad (\text{S.26})$$

$$\hat{\mathcal{U}}_{(1,1,1)}^{\dagger} \hat{\Gamma}^2 \hat{\mathcal{U}}_{(1,1,1)} = \begin{bmatrix} +2ab(\vartheta + \vartheta^*) & -2a^2\vartheta + 2b^2\vartheta^* & 0 & 0 \\ -2a^2\vartheta^* + 2b^2\vartheta & -2ab(\vartheta + \vartheta^*) & 0 & 0 \\ 0 & 0 & +2ab(\vartheta + \vartheta^*) & +2a^2\vartheta^* - 2b^2\vartheta \\ 0 & 0 & +2a^2\vartheta - 2b^2\vartheta^* & -2ab(\vartheta + \vartheta^*) \end{bmatrix} \quad (\text{S.27})$$

$$= \left[\begin{array}{cc|cc} +1/\sqrt{3} & -1/\sqrt{6}-i/\sqrt{2} & 0 & 0 \\ -1/\sqrt{6}+i/\sqrt{2} & -1/\sqrt{3} & 0 & 0 \\ \hline 0 & 0 & +1/\sqrt{3} & +1/\sqrt{6}-i/\sqrt{2} \\ 0 & 0 & +1/\sqrt{6}+i/\sqrt{2} & -1/\sqrt{3} \end{array} \right], \quad (\text{S.28})$$

$$\hat{\mathcal{U}}_{(1,1,1)}^\dagger \hat{\Gamma}^3 \hat{\mathcal{U}}_{(1,1,1)} = \left[\begin{array}{cc|cc} +2(a^2-b^2) & +4ab & 0 & 0 \\ +4ab & -2(a^2-b^2) & 0 & 0 \\ \hline 0 & 0 & +2(a^2-b^2) & -4ab \\ 0 & 0 & -4ab & -2(a^2-b^2) \end{array} \right] \quad (\text{S.29})$$

$$= \left[\begin{array}{cc|cc} +1/\sqrt{3} & +2/\sqrt{6} & 0 & 0 \\ +2/\sqrt{6} & -1/\sqrt{3} & 0 & 0 \\ \hline 0 & 0 & +1/\sqrt{3} & -2/\sqrt{6} \\ 0 & 0 & -2/\sqrt{6} & -1/\sqrt{3} \end{array} \right], \quad (\text{S.30})$$

$$\hat{\mathcal{U}}_{(1,1,1)}^\dagger \hat{\Gamma}^4 \hat{\mathcal{U}}_{(1,1,1)} = \left[\begin{array}{c|ccc} 0 & 0 & 0 & +i \\ 0 & 0 & +i & 0 \\ 0 & -i & 0 & 0 \\ \hline -i & 0 & 0 & 0 \end{array} \right], \quad (\text{S.31})$$

$$\hat{\mathcal{U}}_{(1,1,1)}^\dagger \hat{\Gamma}^5 \hat{\mathcal{U}}_{(1,1,1)} = \left[\begin{array}{c|ccc} 0 & 0 & 0 & -1 \\ 0 & 0 & -1 & 0 \\ 0 & -1 & 0 & 0 \\ \hline -1 & 0 & 0 & 0 \end{array} \right], \quad (\text{S.32})$$

and

$$+m\hat{\mathcal{U}}_{(1,1,1)}^\dagger \left[\begin{array}{cc} 0 & -i\hat{\sigma}_x \\ +i\hat{\sigma}_x & 0 \end{array} \right] \hat{\mathcal{U}}_{(1,1,1)} \\ = \left[\begin{array}{cccc} +m & 0 & 0 & 0 \\ 0 & +m & 0 & 0 \\ 0 & 0 & -m & 0 \\ 0 & 0 & 0 & -m \end{array} \right]. \quad (\text{S.33})$$

First we consider the case of $\vec{k}_W = \pm\sqrt{|m|/2t}(1, 1, 1)^T$. For the $(01\bar{1})$ -domain wall, we introduce a new momentum frame $\vec{\kappa} = (\kappa_X, \kappa_Y, \kappa_Z)^T$ as

$$\vec{k} = \frac{\kappa_X}{\pi} \vec{G}_X + \frac{\kappa_Y}{\pi} \vec{G}_Y + \frac{\kappa_Z}{\pi} \vec{G}_Z \\ = (-\kappa_Y - \kappa_Z, +\kappa_X - \kappa_Y, -\kappa_X - \kappa_Y)^T. \quad (\text{S.34})$$

Then the vector $\vec{d}(\vec{k}) = (d_1, d_2, d_3, d_4, d_5)^T$ is transformed as

$$d_1 = \frac{-1}{\sqrt{3}} (-\kappa_X^2 + \kappa_Y^2), \quad (\text{S.35})$$

$$d_2 = \frac{-1}{\sqrt{3}} \{ +(\kappa_Y + \kappa_Z)\kappa_X + (\kappa_Y + \kappa_Z)\kappa_Y \}, \quad (\text{S.36})$$

$$d_3 = \frac{-1}{\sqrt{3}} \{ -(\kappa_Y + \kappa_Z)\kappa_X + (\kappa_Y + \kappa_Z)\kappa_Y \}, \quad (\text{S.37})$$

$$d_4 = \frac{-1}{2\sqrt{3}} (-\kappa_X^2 + 2\kappa_Y\kappa_X + \kappa_Z^2 + 2\kappa_Y\kappa_Z), \quad (\text{S.38})$$

$$d_5 = \frac{-1}{6} (\kappa_X^2 + 6\kappa_Y\kappa_X - \kappa_Z^2 - 2\kappa_Y\kappa_Z). \quad (\text{S.39})$$

Since k -independent and diagonal terms are absorbed into the chemical potential renormalization, $\hat{\mathcal{H}}_2 = \hat{h}_{4 \times 4}(\vec{k}) + \hat{\mathcal{M}}_2$ may be rewritten after the unitary transformation $\hat{\mathcal{U}}_{(1,1,1)}$ as

$$\begin{aligned} & \hat{\mathcal{U}}_{(1,1,1)}^\dagger \hat{h}_{4 \times 4} \hat{\mathcal{U}}_{(1,1,1)} \\ &= -\frac{2}{3} tk^2 \hat{\sigma}_0 \otimes \hat{\tau}_0 - 2t \hat{\mathcal{U}}_{(1,1,1)}^\dagger \vec{d} \cdot \vec{\Gamma} \hat{\mathcal{U}}_{(1,1,1)} \\ &= -\frac{2}{3} tk^2 \hat{\sigma}_0 \otimes \hat{\tau}_0 - 2t \{ -\kappa_Y^2 \hat{\sigma}_z \otimes \hat{\tau}_0 \\ & \quad + \kappa_Y \kappa_X \left[\hat{\sigma}_x \otimes \hat{\tau}_x + \frac{1}{\sqrt{3}} \hat{\sigma}_x \otimes \hat{\tau}_y \right] \\ & \quad + \frac{\kappa_Y + \kappa_Z}{\sqrt{3}} \kappa_X \left[\sqrt{\frac{3}{2}} \hat{\sigma}_x \otimes \hat{\tau}_z - \frac{1}{\sqrt{2}} \hat{\sigma}_y \otimes \hat{\tau}_0 \right] \\ & \quad + \kappa_Z (\kappa_Z + 2\kappa_Y) \left[-\frac{1}{6} \hat{\sigma}_x \otimes \hat{\tau}_x + \frac{1}{2\sqrt{3}} \hat{\sigma}_x \otimes \hat{\tau}_y \right] \\ & \quad - \frac{1}{\sqrt{3}} \kappa_Z \kappa_Y \left[\frac{2}{\sqrt{3}} \hat{\sigma}_z \otimes \hat{\tau}_0 + \frac{1}{\sqrt{6}} \hat{\sigma}_x \otimes \hat{\tau}_z + \frac{1}{\sqrt{2}} \hat{\sigma}_y \otimes \hat{\tau}_0 \right] \} \end{aligned} \quad (\text{S.40})$$

and

$$\hat{\mathcal{U}}_{(1,1,1)}^\dagger \hat{\mathcal{M}}_2 \hat{\mathcal{U}}_{(1,1,1)} = m \hat{\sigma}_0 \otimes \hat{\tau}_z \quad (\text{S.41})$$

where it is indeed diagonal at $\vec{k}_W = \pm\sqrt{|m|/2t}(1, 1, 1)^T$, which translates to $\kappa_X = \kappa_Z = 0$, and $\kappa_Y = \kappa_Y^{(0)} \equiv \pm\sqrt{|m|/2t}$.

If $m > 0$, the 2nd and 3rd components constitute the Weyl electrons. In other words, for $m > 0$, the diagonal matrix $+2t\kappa_Y^2 \hat{\sigma}_z \otimes \hat{\tau}_0 + m \hat{\sigma}_0 \otimes \hat{\tau}_z$ is non zero for the 1st and 4th components and possibly has zero eigenvalues at $\kappa_X = \kappa_Z = 0$ only for the 2nd and 3rd components, namely at $2t\kappa_Y^2 = m$. Then by extracting the 2nd and 3rd components, the 2×2 hamiltonian is obtained as

$$\begin{aligned}
\hat{h}_{(1,1,1)}^{(+)}(\kappa_X, \delta\kappa_Y, \kappa_Z) &= -\frac{2t}{3}k^2 + \begin{bmatrix} 0 & 0 & 0 & 0 \\ 0 & 1 & 0 & 0 \\ 0 & 0 & 1 & 0 \\ 0 & 0 & 0 & 0 \end{bmatrix} \hat{\mathcal{U}}_{(1,1,1)}^\dagger (-2t\vec{d} \cdot \vec{\Gamma} + m\hat{\Gamma}^{54}) \hat{\mathcal{U}}_{(1,1,1)} \begin{bmatrix} 0 & 0 & 0 & 0 \\ 0 & 1 & 0 & 0 \\ 0 & 0 & 1 & 0 \\ 0 & 0 & 0 & 0 \end{bmatrix} \\
&= -2t\kappa_Y^2 - \frac{4t}{3}\kappa_Z\kappa_Y - \frac{2t}{3}\kappa_Z^2 - 2t(\kappa_Y^2 + \frac{2}{3}\kappa_Z\kappa_Y)\hat{\sigma}_z - \frac{4t}{\sqrt{3}}\kappa_Y\kappa_X\hat{\sigma}_y + \frac{2t}{3}\kappa_Z(\kappa_Z + 2\kappa_Y)\hat{\sigma}_x + m\hat{\sigma}_z \\
&\simeq -2t\left(\kappa_Y^{(0)}\right)^2 - 4t\kappa_Y^{(0)}\delta\kappa_Y - \frac{4t}{3}\kappa_Y^{(0)}\kappa_Z - 2t\left[\left(\kappa_Y^{(0)}\right)^2 + 2\kappa_Y^{(0)}\delta\kappa_Y + \frac{2}{3}\kappa_Y^{(0)}\kappa_Z\right]\hat{\sigma}_z \\
&\quad - \frac{4t}{\sqrt{3}}\kappa_Y^{(0)}\kappa_X\hat{\sigma}_y + \frac{4t}{3}\kappa_Y^{(0)}\kappa_Z\hat{\sigma}_x + m\hat{\sigma}_z
\end{aligned} \tag{S.42}$$

If $m < 0$, zero eigenvalues may appear only for the 1st and 4th components. By extracting the 1st and 4th components, the 2×2 hamiltonian has the form similar to Eq.(S.42) as,

$$\begin{aligned}
\hat{h}_{(1,1,1)}^{(-)}(\kappa_X, \delta\kappa_Y, \kappa_Z) &= 4t\kappa_Y^{(0)} \left\{ -\left(\delta\kappa_Y + \frac{1}{3}\kappa_Z\right)\hat{\sigma}_0 + \left(\delta\kappa_Y + \frac{1}{3}\kappa_Z\right)\hat{\sigma}_z - \frac{1}{\sqrt{3}}\hat{\sigma}_y\kappa_X + \frac{1}{3}\kappa_Z\hat{\sigma}_x + \frac{m(X) + |m|}{4t\kappa_Y^{(0)}}\hat{\sigma}_z \right\}.
\end{aligned} \tag{S.43}$$

Then, surface and domain wall states are obtained by solving Dirac hamiltonian (S.42) and (S.43). For simplicity, we concentrate on a pair of the Weyl points, $\vec{k}_W = \pm(\sqrt{|m|/2t}, \sqrt{|m|/2t}, \sqrt{|m|/2t})^T$, and on a surface or domain perpendicular to $(0, +1, -1)$, namely, $(01\bar{1})$ -surface or domain. In the following discussion, we take the coordination axis along $(0, +1, -1)$ as X -axis. Around these two Weyl points, low-energy quasi-particle excitations are described by the lowest order $\vec{k} \cdot \vec{p}$ -type hamiltonian $\hat{h}_{(1,1,1)}^{(+)}$ up to the linear order in $-i\partial_X$, $\delta\kappa_Y$, and κ_Z ,

$$\begin{aligned}
\hat{h}_{(1,1,1)}^{(+)}(-i\partial_X, \delta\kappa_Y, \kappa_Z) &= 4t\kappa_Y^{(0)} \left\{ -\left(\delta\kappa_Y + \frac{\kappa_Z}{3}\right)\hat{\sigma}_0 + \frac{\kappa_Z}{3}\hat{\sigma}_x + \frac{i}{\sqrt{3}}\hat{\sigma}_y\partial_X \right. \\
&\quad \left. + \left[-\left(\delta\kappa_Y + \frac{\kappa_Z}{3} + \frac{|m|}{4t\kappa_Y^{(0)}}\right) + \frac{m(X)}{4t\kappa_Y^{(0)}}\right]\hat{\sigma}_z \right\}, \tag{S.44}
\end{aligned}$$

for $m(X) = +|m|$, where we introduce a new momentum frame and replace κ_X with $-i\partial_X$. Here the pair of Weyl points is given as $\vec{k}_W = -\kappa_Y^{(0)}(1, 1, 1)^T$ with $\kappa_Y^{(0)} = \pm\sqrt{|m|/2t}$.

Then the two component one-dimensional Dirac equation,

$$\hat{h}_{(1,1,1)}^{(+)}(-i\partial_X, \delta\kappa_Y, \kappa_Z) \begin{bmatrix} \psi_1(X) \\ \psi_2(X) \end{bmatrix} = E \begin{bmatrix} \psi_1(X) \\ \psi_2(X) \end{bmatrix} \tag{S.45}$$

gives description of bound states on the surface or domain walls by carefully choosing the X -dependent “mass” term $m(X)$ as follows. Here we note that the all-out (all-in) domain is described by $m(X) = +|m|$ ($m(X) = -|m|$). We also remind the readers that, for a large enough order parameter $|m|$, the Weyl points are annihilated in pair and the bulk system becomes a trivial magnetic insulator with a charge excitation gap. Note that the mass term

$$m(X) = \begin{cases} +|m| & (X < 0) \\ -|m| & (0 < X) \end{cases}, \tag{S.46}$$

gives a magnetic domain wall at $X = 0$, while the mass term

$$m(X) = \begin{cases} +|M| & (X < 0) \\ +|m| & (0 < X) \end{cases}, \tag{S.47}$$

with $|M| \gg |m|$ mimics a surface between a vacuum ($X < 0$) and the bulk ($X > 0$) at $X = 0$.

Indeed, for the Weyl point with $\kappa_Y^{(0)} < 0$, we obtain the zero modes localized around the surface and the domain wall as

$$\begin{bmatrix} \psi_1(X) \\ \psi_2(X) \end{bmatrix} = \begin{cases} \frac{1}{\sqrt{\lambda_d + \Lambda_d}} \begin{bmatrix} \frac{+1}{\sqrt{2}} \\ \frac{\pm 1}{\sqrt{2}} \end{bmatrix} \begin{cases} e^{+X/\lambda_d} & (X < 0) \\ e^{-X/\Lambda_d} & (0 < X) \end{cases} & (\kappa_Z > 0, \delta\kappa_Y = 0) \text{ (domain wall)} \\ \frac{1}{\sqrt{\lambda_s + \Lambda_s}} \begin{bmatrix} \frac{+1}{\sqrt{2}} \\ \frac{\mp 1}{\sqrt{2}} \end{bmatrix} \begin{cases} e^{+X/\lambda_s} & (X < 0) \\ e^{-X/\Lambda_s} & (0 < X) \end{cases} & (\kappa_Z < 0, \delta\kappa_Y = 0) \text{ (surface)} \end{cases}, \quad (\text{S.48})$$

where inverse penetration lengths are $\lambda_d^{-1} = \kappa_Z/\sqrt{3} > 0$, $\Lambda_d^{-1} = -\sqrt{3}|m|/2\kappa_Y^{(0)} - \kappa_Z/\sqrt{3} > 0$, $\lambda_s^{-1} = -\sqrt{3}(|M| - |m|)/2\kappa_Y^{(0)} + \kappa_Z/\sqrt{3} > 0$, and $\Lambda_s^{-1} = -\kappa_Z/\sqrt{3} > 0$.

Around the Weyl points $\vec{k}_W = \pm(-\sqrt{|m|}/2t, \sqrt{|m|}/2t, \sqrt{|m|}/2t)$, by following similar procedure used for $\hat{h}_{(1,1,1)}^{(\pm)}$, a Dirac hamiltonian describing low-energy quasiparticle excitations is obtained as

$$\begin{aligned} & \hat{h}_{(-1,1,1)}^{(+)}(-i\partial_X, \delta\kappa_Y, \kappa_Z) \\ &= 4t\kappa_Y^{(0)} \left\{ -\left(\frac{\delta\kappa_Y}{3} - \frac{\delta\kappa_Z}{3}\right) \hat{\sigma}_0 - \left(\frac{2\delta\kappa_Y}{3} + \frac{\delta\kappa_Z}{3}\right) \hat{\sigma}_x \right\} \end{aligned}$$

$$+ \frac{i\hat{\sigma}_y}{\sqrt{3}} \partial_X + \left[-\frac{\delta\kappa_Y}{3} + \frac{\delta\kappa_Z}{3} + \frac{m(X) - |m|}{4t\kappa_Y^{(0)}} \right] \hat{\sigma}_z \} \quad (\text{S.49})$$

for $m(X) = +|m|$. The zero modes for the above 2-component Dirac hamiltonian are given as

$$\begin{bmatrix} \psi_1(X) \\ \psi_2(X) \end{bmatrix} = \begin{cases} \frac{1}{\sqrt{\lambda_d + \Lambda_d}} \begin{bmatrix} \frac{+1}{\sqrt{2}} \\ \frac{\pm 1}{\sqrt{2}} \end{bmatrix} \begin{cases} e^{+X/\lambda_d} & (X < 0) \\ e^{-X/\Lambda_d} & (0 < X) \end{cases} & (\delta\kappa_Z < 0, \delta\kappa_Y = 0) \text{ (domain wall)} \\ \frac{1}{\sqrt{\lambda_s + \Lambda_s}} \begin{bmatrix} \frac{+1}{\sqrt{2}} \\ \frac{\mp 1}{\sqrt{2}} \end{bmatrix} \begin{cases} e^{+X/\lambda_s} & (X < 0) \\ e^{-X/\Lambda_s} & (0 < X) \end{cases} & (\delta\kappa_Z > 0, \delta\kappa_Y = 0) \text{ (surface)} \end{cases}, \quad (\text{S.50})$$

where inverse penetration lengths are $\lambda_d^{-1} = -\delta\kappa_Z/\sqrt{3} > 0$, $\Lambda_d^{-1} = -\sqrt{3}|m|/2\kappa_Y^{(0)} + \delta\kappa_Z/\sqrt{3} > 0$, $\lambda_s^{-1} = -\sqrt{3}(|M| - |m|)/2\kappa_Y^{(0)} - \delta\kappa_Z/\sqrt{3} > 0$, and $\Lambda_s^{-1} = \delta\kappa_Z/\sqrt{3} > 0$.

Similarly, we can obtain zero-mode solutions for the Dirac equations $\hat{h}_{(1,1,1)}^{(-)}\vec{\psi} = E\vec{\psi}$ and $\hat{h}_{(-1,1,1)}^{(-)}\vec{\psi} = E\vec{\psi}$. These solutions are summarized in Figure 2b of the main article and Figure 6.

IV. PAIR-ANNIHILATION OF WEYL ELECTRONS AT A L-POINT

To fully understand the pair-annihilation of bulk Weyl points and formation of the closed loop of the Fermi

surfaces on the domain walls, we need to examine the structure of the original hamiltonian, $\hat{K}_0(\vec{k}) + \hat{Z}_0(\vec{k})$, around the L-point $(\pi/4a, \pi/4a, \pi/4a)$, where the pair-annihilation occurs, beyond the applicability of the lowest order $\vec{k} \cdot \vec{p}$ -theory developed above.

Here we expand the 8×8 Bloch hamiltonian around the L-point by setting $\vec{k} = (\pi/4a, \pi/4a, \pi/4a) + (\delta k_x, \delta k_y, \delta k_z)$,

$$\hat{K}_0 = -2t\hat{\sigma}_0 \begin{bmatrix} 0 & 1 & 1 & -\delta k_z - \delta k_x \\ 1 & 0 & 1 & -\delta k_y - \delta k_z \\ 1 & 1 & 0 & -\delta k_x - \delta k_y \\ -\delta k_z - \delta k_x & -\delta k_y - \delta k_z & -\delta k_x - \delta k_y & 0 \end{bmatrix} + \mathcal{O}(t\delta k^2), \quad (\text{S.51})$$

and

$$\hat{Z}_0 = \sqrt{2}i\zeta \begin{bmatrix} 0 & +\hat{\sigma}_x + \hat{\sigma}_y & -\hat{\sigma}_y - \hat{\sigma}_z & 0 \\ -\hat{\sigma}_x - \hat{\sigma}_y & 0 & \hat{\sigma}_z + \hat{\sigma}_x & 0 \\ \hat{\sigma}_y + \hat{\sigma}_z & -\hat{\sigma}_z - \hat{\sigma}_x & 0 & 0 \\ 0 & 0 & 0 & 0 \end{bmatrix}$$

$$+ \mathcal{O}(\zeta\delta k) \quad (\text{S.52})$$

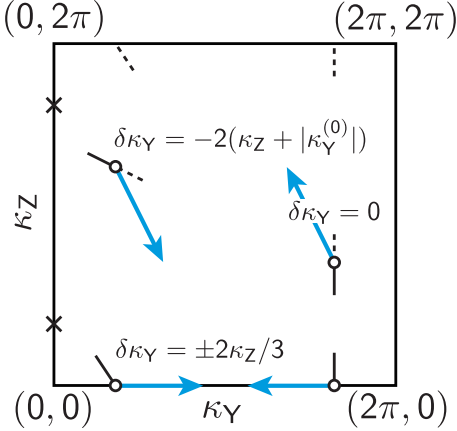


FIG. 6: **Summary of solutions for the Dirac equations.** Loci of the domain-wall (surface) states are represented by solid (broken) lines, which are obtained as zero modes of the Dirac hamiltonians, $\hat{h}_{(1,1,1)}^{(\pm)}$, given in equations (S.68) and (S.69), and $\hat{h}_{(-1,1,1)}^{(\pm)}$ (see equation (S.74)). Open circles and crosses illustrate the Weyl points projected to (κ_Y, κ_Z) -plane.

It is easy to determine qualitative properties of the 2-component Dirac equations derived from the 8×8 hamiltonian as follows. First, we examine a level crossing at the L-point under the influence of \hat{M}_0 , which directly corresponds to the pair-annihilation of the Weyl points. Level scheme at the L-point for $\delta\vec{k} = \vec{0}$ and $m = 0$ is given by 4 doublets, $E = -t - \sqrt{2}\zeta \pm \sqrt{9t^2 - 6\sqrt{2}t\zeta + 6\zeta^2}$, $2t + 2\sqrt{2}\zeta$, and 0 (see Figure 7a). These doublets at the L-point are classified by the irreducible representation of the point group D_{3d} , as two Kramers pairs $E_{1/2u}$ at $E = -t - \sqrt{2}\zeta \pm \sqrt{9t^2 - 6\sqrt{2}t\zeta + 6\zeta^2}$, one doublet $E_{3/2u}$ at $E = 2t + 2\sqrt{2}\zeta$, and one Kramers pair $E_{1/2g}$ at $E = 0$, if we choose the site $(0, 0, 0)$ in Figure 1b as the center of inversion, which corresponds to the 7th and 8th components of the 8×8 Bloch hamiltonian. When we introduce a nonzero order parameter m , namely, nonzero \hat{M}_0 , and break the time-reversal symmetry, the degeneracies of the four doublets are all lifted. Then, if $2t + 2\sqrt{2}\zeta > 0$ holds, the level crossing between the two states occurs at $|m| = m_c$, one originally from the state at $E = 2t + 2\sqrt{2}\zeta$

and splits downward for $m \neq 0$ and the other originally from the state at $E = 0$ and splits upward for $m \neq 0$ (see Figure 7a). The classification of the 4 doublets tells us an important fact further: Although the all-in/all-out order parameter described by \hat{M}_0 lifts the degeneracy of the doublets $E_{1/2u}$ at $E = 2t + 2\sqrt{2}\zeta$ and the Kramers pair $E_{1/2g}$ at $E = 0$, the all-in/all-out order \hat{M}_0 does not hybridize them. Furthermore, \hat{M}_0 does not create matrix elements among $E_{1/2g}$ and other doublets. Therefore, the low-energy effective theory around the pair-annihilation of the Weyl points only consists of these two doublets, namely, $E_{1/2u}$ and $E_{1/2g}$.

Now, we focus on the $(01\bar{1})$ -domain wall for illustrative purpose and note that, up to linear orders in κ_X , $\delta\kappa_Y$, and κ_Z , 2×2 -Dirac hamiltonians describing low energy physics do not contain terms proportional to $\delta\kappa_Y$, due to the point symmetry of the electronic band around $\vec{k} = (\pi/4a, \pi/4a, \pi/4a)$. Here we introduce a new oblique coordinate $(\kappa_X, \delta\kappa_Y, \kappa_Z)$ through $(\delta k_x, \delta k_y, \delta k_z) = (-\delta\kappa_Y - \kappa_Z, +\kappa_X - \delta\kappa_Y, -\kappa_X - \delta\kappa_Y)$, for the $(01\bar{1})$ -domain wall. It is easy to see that, along the (111) -direction, the band dispersion shows a quadratic band crossing at the pair-annihilation of the Weyl points. In other words, along the κ_Y -axis parallel to the (111) -direction, the linear dispersion disappears. Therefore, in general, the pair of the low energy 2×2 Dirac hamiltonian around the L-point is given as

$$\begin{aligned} \hat{h}_L^{(\pm)} = & -[m \mp |m_c|] \hat{\sigma}_z + \left(v_{Xx}^{(\pm)} \hat{\sigma}_x + v_{Xy}^{(\pm)} \hat{\sigma}_y \right) \kappa_X \\ & + \left(v_{Zx}^{(\pm)} \hat{\sigma}_x + v_{Zy}^{(\pm)} \hat{\sigma}_y \right) \kappa_Z, \end{aligned} \quad (S.53)$$

where velocities $v_{Xx}^{(\pm)}$, $v_{Xy}^{(\pm)}$, $v_{Zx}^{(\pm)}$, and $v_{Zy}^{(\pm)}$ are introduced and $|m_c| = t + \sqrt{2}\zeta$ is the critical value of m for the pair-annihilation of the Weyl points. Here we emphasize that the above set of the Dirac hamiltonian exploits the low energy Hilbert space $E_{1/2u} \oplus E_{1/2g}$. The solution of Eq.(S.53) as a function of m is illustrated in Figure 7b, which has of course the same structure as Figure 7a in the low energy region. By replacing m and κ with $m(X)$ and $-i\partial_X$ respectively, we obtain the following 1D Dirac equation,

$$\hat{h}_L^{(\pm)}(X) = -[m(X) \mp |m_c|] \hat{\sigma}_z - i\tilde{v}_X^{(\pm)} \left(\cos \varphi_X^{(\pm)} \hat{\sigma}_x + \sin \varphi_X^{(\pm)} \hat{\sigma}_y \right) \partial_X + \tilde{v}_Z^{(\pm)} \left(\cos \varphi_Z^{(\pm)} \hat{\sigma}_x + \sin \varphi_Z^{(\pm)} \hat{\sigma}_y \right) \kappa_Z, \quad (S.54)$$

where velocities, $\tilde{v}_X^{(\pm)}$ and $\tilde{v}_Z^{(\pm)}$, and phases, $\varphi_X^{(\pm)}$ and $\varphi_Z^{(\pm)}$, are defined through $\tilde{v}_X^{(\pm)} e^{i\varphi_X^{(\pm)}} = v_{Xx}^{(\pm)} + i v_{Xy}^{(\pm)}$ and $\tilde{v}_Z^{(\pm)} e^{i\varphi_Z^{(\pm)}} = v_{Zx}^{(\pm)} + i v_{Zy}^{(\pm)}$.

Here the $(01\bar{1})$ -domain wall with an all-out domain for $X < 0$ and an all-in domain for $X > 0$ is described by

the following X -dependent mass term,

$$m(X) = +|m| \theta(-X) - |m| \theta(+X), \quad (S.55)$$

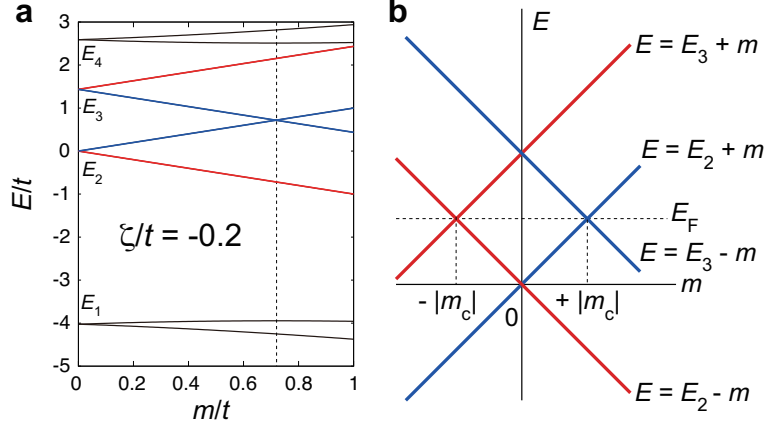


FIG. 7: **Level scheme of L-point and its dependence on all-in/all-out order parameter.** **a**, Level splitting at L-point due to finite order parameter m . Here the 4 doublets are located at $E_1 = -t - \sqrt{2}\zeta - \sqrt{9t^2 - 6\sqrt{2}t\zeta + 6\zeta^2}$, $E_2 = 0$, $E_3 = 2t + 2\sqrt{2}\zeta$, and $E_4 = -t - \sqrt{2}\zeta + \sqrt{9t^2 - 6\sqrt{2}t\zeta + 6\zeta^2}$, for $m = 0$. The vertical broken line shows $m = |m_c|$ for which the bulk Weyl points are annihilated in pairs. The two blue (red) states show the states adiabatically connected to the states that form the domain-wall state at $m = m_c$ ($m = -m_c$). Namely, the two blue (red) lines indicate the two solutions of the 2×2 low-energy Dirac hamiltonian $\hat{h}_L^{(+)} (\hat{h}_L^{(-)})$ (S.53). See **b** for more focused illustration. **b**, Level splitting focused on the low-energy states, around the chemical potential. The blue states around the Fermi level E_F form a domain-wall state confined in the side of the positive magnetization, while the red states around the Fermi level are confined in the opposite $m < 0$ side of the domain wall (See discussions below equation (S.57)).

which is justified from the level scheme splitting illustrated in Figure 7b.

Then the solution for the 1D Dirac equation $\hat{h}_L^{(+)}(X)$, after the pair-annihilation of the Weyl points ($|m| > |m_c|$),

$$\hat{h}_L^{(+)}(X)\vec{\psi} = 0 \cdot \vec{\psi}, \quad (\text{S.56})$$

is given by

$$\vec{\psi}(X) = \frac{1}{\sqrt{\lambda_{\text{dL}} + \Lambda_{\text{dL}}}} \left[\theta(-X)e^{+X/\lambda_{\text{dL}}} + \theta(+X)e^{-X/\Lambda_{\text{dL}}} \right] \times \begin{bmatrix} 1/\sqrt{2} \\ ie^{i\varphi_X}/\sqrt{2} \end{bmatrix}, \quad (\text{S.57})$$

where the inverse penetration lengths are $\lambda_{\text{dL}}^{-1} = (|m| - |m_c|)/\tilde{v}_X^{(+)} > 0$ and $\Lambda_{\text{dL}}^{-1} = |m|/\tilde{v}_X^{(+)} > 0$, along the locus defined by $\kappa_Z = 0$. The above solution is mainly confined in the side of the positive magnetization $m > 0$. By solving the other 1D Dirac equation $\hat{h}_L^{(-)}(X)\vec{\psi} = 0 \cdot \vec{\psi}$, the domain-wall state confined in the side of the negative magnetization $m < 0$ is obtained in the same manner.

We note that, for $\kappa_Z = 0$, an operator,

$$\hat{\Gamma} = -\sin \varphi_X^{(+)} \hat{\sigma}_x + \cos \varphi_X^{(+)} \hat{\sigma}_y, \quad (\text{S.58})$$

becomes a chiral one for the above 1D Dirac equation that satisfies the following identities,

$$\hat{\Gamma}^\dagger \hat{h}_L^{(+)}(X) \hat{\Gamma} = -\hat{h}_L^{(+)}(X), \quad (\text{S.59})$$

and $\hat{\Gamma}^\dagger \hat{\Gamma} = 1$. Here, we also note that, in the above derivation, the chemical potential is assumed to be pinned at the Weyl points.

Therefore, the domain-wall zero modes given by the solution equation (S.57) is protected by the chiral operator $\hat{\Gamma}$, in other words, protected by the chiral symmetry of $\hat{h}_L^{(+)}(X)$ with $\kappa_Z = 0$ (see Ref.2). The classification of the topological insulators introduced in Ref.2 tells that the 1D chiral Dirac equations derived for the low-energy physics around the L-point describe the AIII Chern insulators. From the above derivation, our 1D Dirac equations turn out to be chiral, at least, around the L-point. As long as the chemical potential is pinned at the Weyl point or the center of the bulk gap, then the zero modes are preserved.

Here we note that, although there exists a substantial similarity of the present Dirac hamiltonian to the well-studied Su-Schrieffer-Heeger hamiltonian (see Ref.25), namely, the chiral symmetry shared by both hamiltonian, the latter effective hamiltonian for polyacetylene and other conducting polymers additionally possesses the time-reversal and particle-hole symmetries. In addition to the difference in the symmetric properties, our 1D chiral Dirac equations describe the domain-wall states at a specified κ . By a variation of κ , they constitute 2D Fermi surfaces on the domain walls, while the edges of the Su-Schrieffer-Heeger model are genuinely zero dimensional ones.